# Deep Orographic Storms over the Sierra Nevada. Part II: The Precipitation Processes

JOHN D. MARWITZ

*Department of Atmospheric Science, University of Wyoming, Laramie, WY 82071*

(Manuscript received 22 October 1984, in final form 8 August 1986)

ABSTRACT

The thermodynamic and kinematic structure of two stable orographic storms were described in Part I based on instrumented aircraft data and single Doppler radar data. The precipitation processes in these storms are described in this paper. The storms were deep with cloud top temperatures of about −25°C. Below the melting level the cloud droplet population was continental with a mean droplet diameter < 10 μm. Above the melting level the cloud droplet population was maritime with mean droplet diameters of 20 to 30 μm. Near the −5°C level a peak in ice crystal concentration of 30 to 200 $L^{-1}$ was observed. Since most of the ice crystals were needles, a rime-splintering secondary ice crystal production process as generally described by Hallett and Mossop was probably occurring.

Calculations of the condensation supply rates were compared with the depletion rates by deposition and accretion. The depletion rates by deposition were less than half the condensation supply rates, and the liquid water contents remained very low. Accretion is deduced to be the dominant process, which acts to deplete the condensate to near zero. Deep, stable orographic storms over the Sierra barrier, therefore, develop an efficient glaciation process.

## 1. Introduction

Deep, stable orographic clouds produce a majority of the precipitation over the Sierra barrier. The Sierra Cooperative Pilot Project (SCPP) is investigating whether cloud seeding can be used to augment the precipitation over the Sierra barrier. The thermodynamic and kinematic structures of two deep, stable orographic storms were described in Part I (Marwitz, 1987).

The precipitation rates from these two storms were ~4 mm $h^{-1}$ and the forced ascent rates were ~0.4 m $s^{-1}$. The observed hydrometeor characteristics and the inferred precipitation processes are described in this article. The total ice crystal populations were distributed super-exponentially. (A super-exponential distribution of hydrometeors is defined as one in which there are an excess of particles with diameters less than ~1 mm over the concentration given by fitting an exponential function for diameter > 1 mm.) The excess of small particles were mostly needles which appeared to result from a rime-splintering process. Only a small amount of supercooled water (<0.2 g $m^{-3}$) was observed in these clouds and the cloud droplet concentration was less than 50 $cm^{-3}$.

The objective of this article is to understand the precipitation process in deep, stable orographic storms over the Sierra Nevada. The relative roles of hydrometeor growth by diffusion and accretion will be established. The role of ice multiplication in these clouds will also be examined.

The condensation supply rates were calculated from the thermodynamic and kinematic data. A bulk parameterization technique (Lin et al., 1983) was used to calculate the relative values of deposition and accretion depletion rates. The technique uses exponential ice crystal distributions partitioned into cloud ice and precipitation ice. The observed super-exponential distributions were approximated by an exponential cloud ice spectrum and an exponential precipitation ice spectrum. In the model cloud ice grows by deposition and the precipitation ice grows by deposition and by accretion of supercooled water. The relative values of deposition and accretion were compared to the condensation supply rates.

The cloud water was measured by integrating the cloud droplet spectrum from a Forward Scattering Spectrometer Probe (FSSP). In general, the cloud water content was below the threshold of the hot-wire probes. Three optical array probes were used to record the size distributions of hydrometeors. The one-dimensional Optical Array Cloud Spectrometer (OAP-200X) operates from 12.5 to 187.5 μm by 12.5 μm intervals. The two-dimensional Optical Array Cloud Probe (OAP-2D-C) views a sample width of 800 μm and operates by 25 μm intervals. The two-dimensional Optical Array Precipitation Probe (OAP-2D-P) views a sample width of 6400 μm and operates by 200 μm intervals. (All of the optical array probes are manufactured by Particle Measuring Systems, Inc., Boulder, Colorado.) The size range measured by the 2D-C and 2D-P can be either in the lateral dimension (perpendicular to the flight path), or, if the time slice data is used, the longitudinal dimension (along the flight path). In this study we use the longitudinal dimension, allowing the size

... Meteorological Society

TABLE 1. Size classes ($\mu$m) for PMS Optical Array Probes.

| Class | 1D-C | 2D-C | 2D-P |
|---|---|---|---|
| 1 | 0–12.5 | <50 | 200–400 |
| 2 | 12.5–25 | 50–100 | 400–600 |
| 3 | 25–37.5 | 100–150 | 600–800 |
| 4 | 37.5–50 | 150–200 | 800–1000 |
| 5 | 50–67.5 | 200–250 | 1000–1250 |
| 6 | 67.5–75 | 250–300 | 1250–1500 |
| 7 | 75–87.5 | 300–400 | 1500–1750 |
| 8 | 87.5–100 | 400–500 | 1750–2000 |
| 9 | 100–112.5 | 500–600 | 2000–2250 |
| 10 | 112.5–125 | 600–800 | 2250–2500 |
| 11 | 125–137.5 | 800–1000 | 2500–2750 |
| 12 | 137.5–150 | 1000–1250 | 2750–3000 |
| 13 | 150–167.5 | 1250–1500 | 3000–3500 |
| 14 | 167.5–175 | 1500–2000 | 3500–4000 |
| 15 | 175–187.5 | 2000–2500 | 4000–4500 |
| 16 | | 2500–3000 | 4500–5000 |
| 17 | | 3000–4000 | 5000–6000 |
| 18 | | 4000–5000 | 6000–8000 |
| 19 | | 5000–6000 | 8000–10000 |
| 20 | | >6000 | >10000 |

range to thereby be increased to much larger sizes. Both 2D probes were vertically oriented.

Data from the FSSP were divided into 15 intervals of 3 $\mu$m each. Concentrations were corrected for dead time and coincidence errors. The 1D and 2D probe data were divided into 15 and 20 size classes, respectively (see Table 1). The size classes were chosen to give a more uniform concentration in each size class and thereby to give better sampling statistics at the larger size classes.

During 2D data processing, artifacts were rejected according to the criteria in Table 2. All other images were accepted as real particles regardless of where the center of the particle might lie. The sample volume was adjusted for individual images by increasing the effective array width by the maximum longitudinal dimension. This allows for half of each particle to be outside the sampling area. No depth of field correction was applied, probably resulting in an undercounting of particles in the smallest few size classes.

## 2. Observed hydrometeor characteristics

### *a. 25 February 1983 case*

The concentrations of hydrometeors detected by the 2D-C probe are presented in Fig. 1a. A few key isotherms are indicated on the figure. Below the melting layer,[1] the concentration was $<3$ L$^{-1}$. Numerous large aggregates were present immediately above the melting level. A peak concentration ($>100$ L$^{-1}$) was located near the $-5$°C level. Examination of the images revealed that many of these hydrometeors were needles. There were no graupel particles present, but many of the particles were moderately rimed with some heavily rimed particles present near the barrier. Since the peak concentration of ice particles was near the $-5$°C level, the concentration exceeded the Fletcher (1962) ice nuclei curve by 5 or 6 orders of magnitude and many of them were needles. This indicates that a Hallett and Mossop (1974) secondary ice crystal production (SICP) process was probably active.

The cloud water content over the barrier is presented in Fig. 1b. The cloud water contents were integrated from the FSSP cloud droplet spectra. The FSSP will properly size cloud droplets, but in the presence of ice particles the laser light is scattered in an unpredictable manner such that an ice crystal is sized randomly. If an individual ice crystal shatters on the probe tip, it may produce several "droplets." This occurrence is random and is likely to occur in high concentrations of graupel. Two criteria were imposed, therefore, on the FSSP spectra to discriminate ice from cloud droplets. To be considered a spectrum of cloud droplets, the concentration must exceed 10 cm$^{-3}$ for at least 30 s (10 000 ice crystals per liter is unrealistic), and the size distribution must display a distinct peak in concentration. FSSP concentrations $<$ 10 cm$^{-3}$ which are uniformly distributed in size are likely caused by ice but can be water droplets. When the FSSP concentration is $<$10 cm$^{-3}$ but displays a distinct size peak, this may indicate cloud droplets. The cloud water exceeded 0.1 g m$^{-3}$ above the melting level and close to the mountain barrier. A few values exceeding 0.2 g m$^{-3}$ were encountered very close to the barrier at about $-2$°C.

The concentrations of particles detected by the FSSP probe are presented in Fig. 1c. There were a couple of regions away from the barrier where the concentration

TABLE 2. 2D-C and 2D-P artifact rejection criteria.

1. Streakers (usually, water shedding across the upstream edge of the probe and across the aperture) are rejected if they are six times as long (longitudinal dimension) as they are wide (lateral dimension). Images are also rejected as streakers if the longitudinal dimension is ⩾ three times the lateral dimension and the images are either < eight elements wide or overlay the edge of the scan region.
2. Cases in which the probe recording circuitry is triggered but no elements are recorded as shadowed (so-called zero-area images) are rejected. These often correspond to true objects near the minimum size detectable by the probe.
3. Images resulting from particles splashing off the edges of the aperture are eliminated by calculating the Poisson distributed average longitudinal distance between particles based on concentration. Those particles are rejected that pass through the beam at times less than the time corresponding to the average distance.
4. Images having more than two discontinuous parts are rejected.

[1] Stewart et al. (1984) have shown that the melting layer is from 0°C down to +3°C for those Sierra storms which have aggregates and some rime.

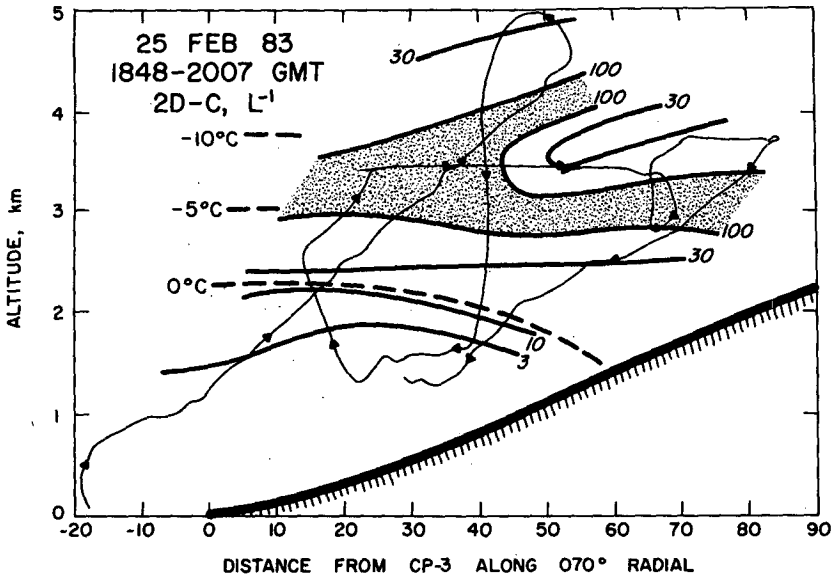


FIG. 1a. Vertical cross sections of King Air data on 25 February 1983 along the 070° radial from the CP-3 radar. The crest line is near 100 km, and the CP-3 radar was near the upwind edge of the barrier. The analyzed fields are 2D-C concentration of hydrometeors. A few key isotherms are indicated. The flight track is shown with arrows at 5-min intervals.

exceeded 10 $cm^{-3}$, but the size distribution did not display a distinct peak in particle size. Therefore, significant numbers of those particles were probably ice. Close to the barrier and below the melting layer the FSSP concentration exceeded 100 $cm^{-3}$. They decreased to <10 $cm^{-3}$ above the −4°C level.

Several droplet spectra from the FSSP data are presented in Fig. 2. These data were obtained during the descent along the barrier at minimum obstruction clearance altitude from the −3°C level down to the 2°C level and then during the initial part of the climb back through the 1°C level. The temperature, mean droplet diameter, droplet concentration and cloud water content are tabulated for each spectrum. At the −3°C level the mean diameter was 27.5 $\mu$m and the concentration was 9 $cm^{-3}$. During the aircraft descent

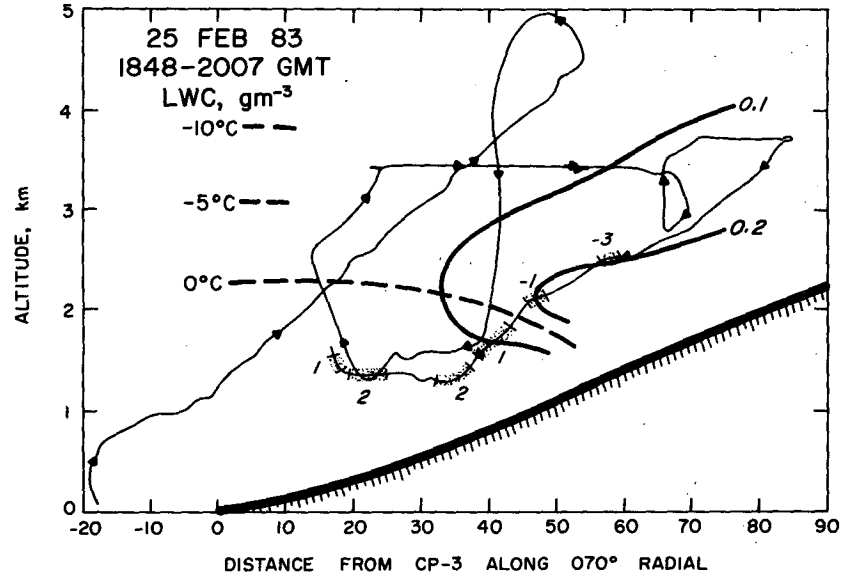


FIG. 1b. Integrated cloud water content from FSSP spectra. The flight intervals and mean temperatures for the cloud droplet spectra shown in Fig. 2 are indicated.

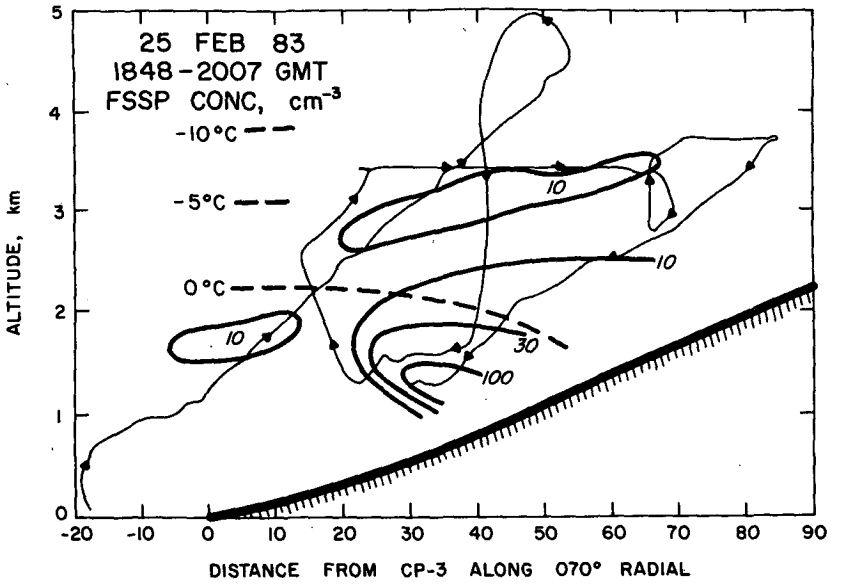


FIG. 1c. Concentration of FSSP detected hydrometeors.

from the 0°C level to the 2°C level, the mean diameter decreased to 7.6 $\mu$m and the concentration increased to 134 cm$^{-3}$. The cloud water content was >0.1 g m$^{-3}$ above the 0°C level and <0.1 g m$^{-3}$ below the 0°C level. During the aircraft climb back through the 1°C level, the mean diameter increased from 6.7 to 13.5 $\mu$m. Above the 0.5°C level no droplets were detected.

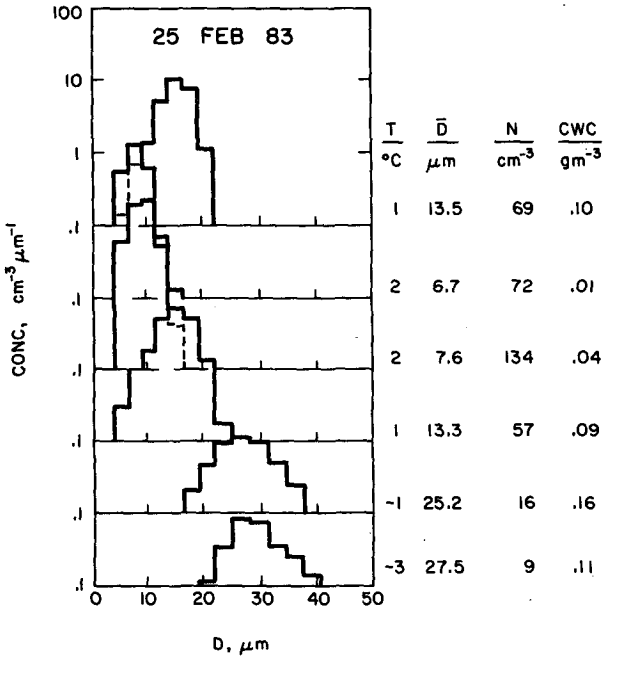


FIG. 2. Cloud droplet spectra from the FSSP for the flight intervals indicated in Fig. 1b. The mean temperature ($T$), mean diameter ($D$), concentration ($N$), and integrated cloud water content (CWC) are tabulated for each spectrum.

It is interesting to compare the cloud water content (Fig. 1b), the cloud droplet concentrations (Fig. 1c), and the cloud droplet distributions (Fig. 2). In the region where the LWC was >0.2 g m$^{-3}$, the cloud droplet concentrations were ~20 cm$^{-3}$ with a mean droplet diameter of 27 $\mu$m. In the region where the cloud droplets were >100 cm$^{-3}$, the mean droplet diameter of 7 $\mu$m only gives a LWC of 0.02 g m$^{-3}$.

### *b. 30 March 1982 case*

The concentration of hydrometeors detected by the 2D-C probe are presented in Fig. 3a. The pattern is similar with respect to temperature to that of the 2D-C hydrometeors detected on 25 February 1983 (Fig. 1a). The concentration of particles below the melting layer was <3 L$^{-1}$. Near the −5°C level a peak concentration > 30 L$^{-1}$ was observed. Near the barrier this peak concentration was lifted up and over the barrier and appeared to begin its descent upwind of the crest. The crest of the airflow was also in this region (Part I, Fig. 8d). Many of the images within the >30 L$^{-1}$ region were needles. Just above the melting layer where the concentration was decreasing rapidly with decreasing altitude, the dominant image was that of large aggregates or snowflakes. Near the barrier and above the melting layer, the crystals were moderately to heavily rimed. The Hallett–Mossop SICP process was likely operating as in the previous case.

The profile of cloud water content as integrated from the FSSP probe data is presented in Fig. 3b. Two separate regions of low liquid water content were identified. The region at an altitude of 3 km over the foothills contained some supercooled cloud water. The temperature in this region was −12°C. This region of cloud water was probably caused by the initial ascent of the

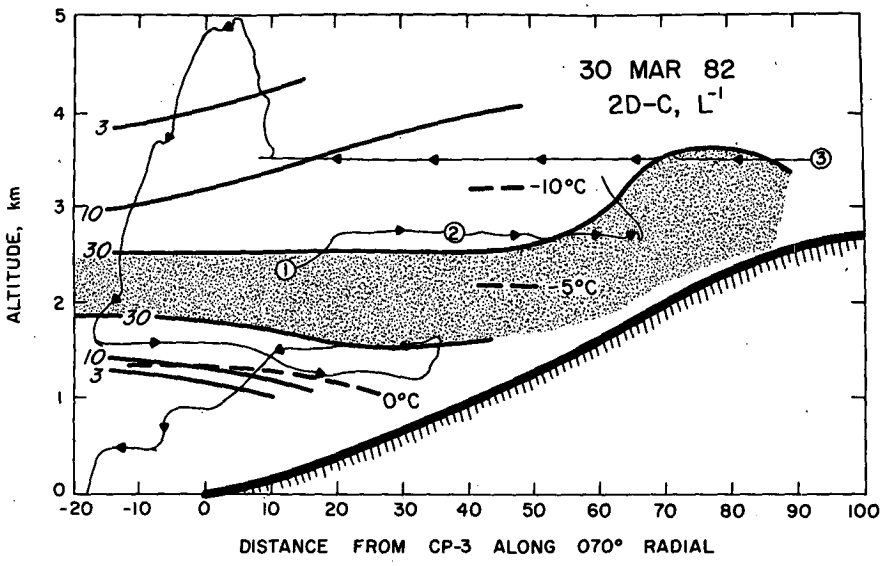


FIG. 3a. Vertical cross sections of King Air data on 30 March 1982 along the 070° radial from the CP-3. The crest line is near 100 km and the CP-3 was near the upwind edge of the barrier. The analyzed fields are 2D-C concentration of hydrometeors. A few key isotherms are indicated. The flight track is shown with arrows at 5-min intervals.

airflow over the barrier (see Part I, $\theta_e$ = 300 K, Fig. 5c). We will see later that this condensate was probably depleted by depositional growth on the existing crystals. The concentration of FSSP detected particles was 30 to 80 cm$^{-3}$ with the mean droplet diameter ~6.0 $\mu$m at the upwind edge and ~10.6 $\mu$m at the downwind edge.

The second region of supercooled water was near the barrier (Fig. 4). Flight segment 3 began near the crest line at −13°C and the FSSP detected only 4 particles per cm$^{-3}$. Since the particles were restricted in size from 22 to 41 $\mu$m, they may have been cloud droplets. Flight segment 2 penetrated to within 1 km above the barrier at the −9°C level. The concentration of particles was 17 cm$^{-3}$ with a mean droplet diameter of 11.7 $\mu$m. Some of the detected particles with sizes greater than 21 $\mu$m may have resulted from ice crystals since the tail of the distribution is rather flat. The concentration of particles and distinct peak in concentration for particles less than 20 $\mu$m indicate that most of

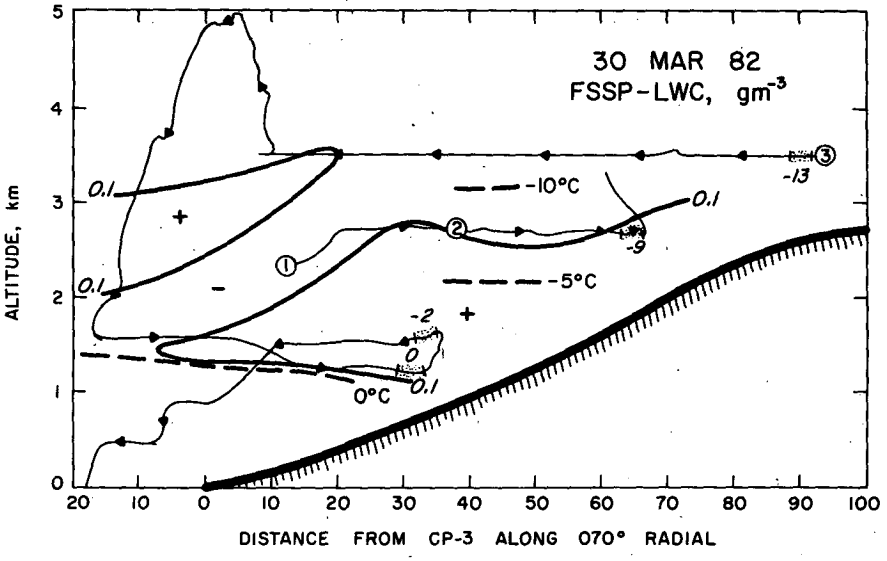


FIG. 3b. Integrated cloud water content from FSSP spectra. The flight intervals and mean temperatures for the cloud droplet spectra shown in Fig. 4 are indicated.

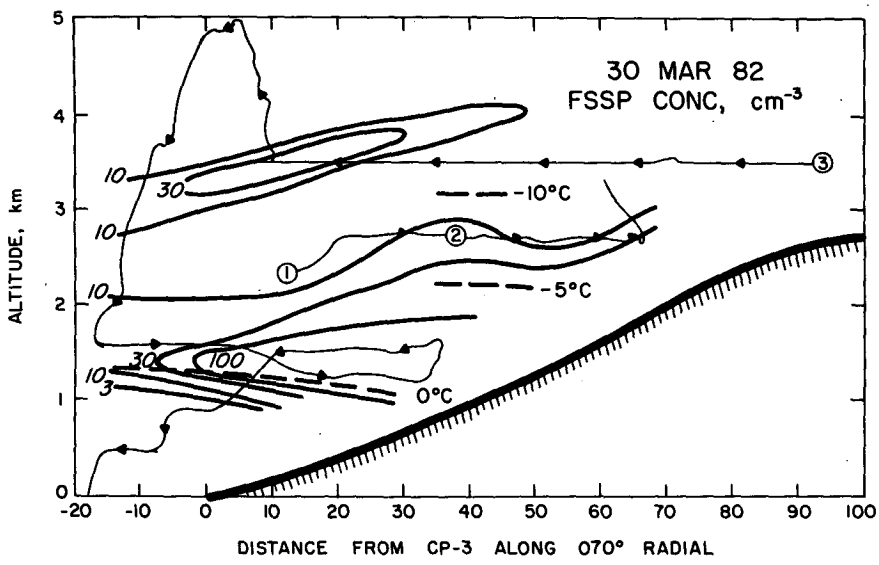


FIG. 3c. Concentration of FSSP detected hydrometeors.

the particles were cloud droplets. Close to the barrier, the cloud droplet distribution at −2°C had a mean diameter of 10.6 μm and a concentration of 102 $cm^{-3}$. At 0°C the mean diameter was 7.3 μm and the concentration was 129 $cm^{-3}$.

Although we did not fly continuously along the minimum obstruction clearance altitude from the crest down to below the melting layer, the available FSSP data near the barrier are consistent with those collected on 25 February 1983. The available data seem to indicate that the concentration of FSSP particles was ~125 $cm^{-3}$ near the 0°C level with mean droplet diameters of 7 μm. Above the melting layer the FSSP concentrations decreased to <10 $cm^{-3}$ as the mean droplet diameters increased to ~30 μm in the downwind direction. Just upwind of the crest it appears that almost all the cloud water was depleted by deposition and/or accretion.

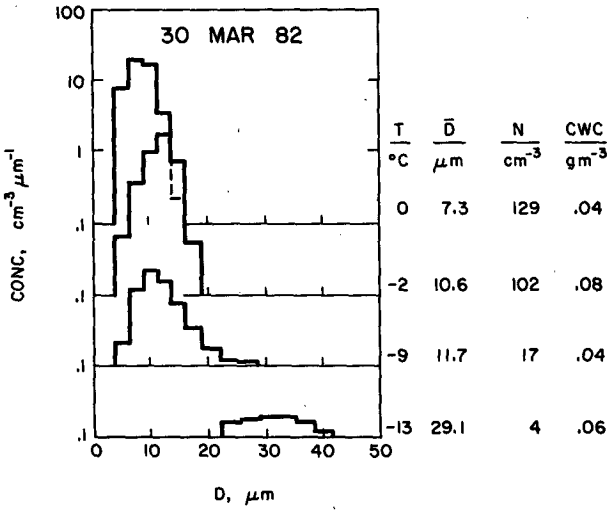


FIG. 4. Cloud droplet spectra from the FSSP for the flight intervals indicated in Fig. 3b. The mean temperature ($T$), mean diameter ($D$), concentration ($N$), and integrated cloud water content (CWC) are tabulated for each spectrum.

## 3. Model of the precipitation process

The condensation supply rate is given by Haltiner and Williams (1980, p. 309).

$$\frac{dq_s}{dt} = \frac{gq_s}{R}\frac{C_pR_vT - KR}{C_pR_vT^2 + q_sK^2}W \tag{1}$$

where $g$ is the acceleration due to gravity, $q_s$ is saturation mixing ratio, $R$ is the gas constant for air, $C_p$ is the specific heat capacity for air, $R_v$ is the gas constant for vapor, $T$ is temperature, $K$ is the latent heat of condensation, and $W$ is the vertical velocity.

The deposition depletion rate onto a spectrum of cloud ice is given by

$$\frac{dM_c}{dt} = \int_0^\infty \frac{dm}{dt}N_c(L)dL \tag{2}$$

where $dm/dt$ is the deposition rate onto a single ice particle of mass, $m$, and is given by

$$\frac{dm}{dt} = \frac{4\pi C}{A+B}(S_e - 1) \tag{3}$$

where $C$ is the capacitance and varies from $C = L/2$ for a sphere to $C = L/\pi$ for a circular disk to $C = L/\ln(2L/b)$ for a needle. The length is $L$ and the semi-minor axis of the needle is $b$. Oblate and prolate spheroids have more complicated functions describing the value of $C$. The value of $C$ for circular disks was used

since it lies between the extremes for all shapes and is within 20% of the extreme values. The value $S_e - 1$ is the supersaturation with respect to an ice surface. The air is assumed saturated with respect to water. Since the condensation supply rate nearly always exceeds the deposition depletion rate (as we shall see later), the atmosphere must be saturated with respect to water. The presence of a few cloud droplets confirms the water saturation assumption. In (3) $A$ and $B$ are conventional terms defined in most cloud physics textbooks (e.g., Pruppacher and Klett, 1980, p. 448).

The parameter $N_c(L)$ is the least-squares fitted exponential distribution to the observed 1D-C hydrometeor spectra.

$$N_c(L) = N_c(0) \exp(-\lambda_c L_c) \tag{4}$$

where $N_c(0)$ is the value of $N_c$ at $L = 0$. The slope parameter is $\lambda_c$. Substituting (3) and (4) into (2) and integrating gives the deposition depletion rate on cloud ice.

$$\frac{dM_c}{dt} = GN_c(0)\lambda_c^{-2} \tag{5}$$

where

$$G = \frac{4(S_e - 1)}{A + B}.$$

The deposition depletion rate onto a spectrum of precipitation ice is given by

$$\frac{dM_p}{dt} = \int_0^\infty F \frac{dm}{dt} N_p(L) dL. \tag{6}$$

Here $F$ is the ventilation factor which is given by Thorpe and Mason (1966)

$$F = 0.65 + 0.37\ \mathrm{Re}^{0.5} \tag{7}$$

where Reynolds number (Re) is $VL\rho/\mu$. Constants are in MKS units. The air density is $\rho$ and $\mu$ is dynamic viscosity of air. From Locatelli and Hobbs (1974) $V$ is the mass weighted fallspeed for aggregates of dendrites

$$V = aL^b(p_0/p)^{0.4} \tag{8}$$

where $a = 1.139$, $b = 0.11$ and the factor $(p_0/p)^{0.4}$ allows for the change in fallspeed with air pressure (Foote and du Toit, 1969). The $N_p(L)$ is similar to (4)

$$N_p(L) = N_p(0) \exp(-\lambda_p L_p) \tag{9}$$

where $N_p(0)$ is the value of $N_p(L)$ at $L = 0$. The slope parameter is $\lambda_p$. The exponential distribution is fitted to the observed 2D-P hydrometeor spectra for 0.5 mm $< L <$ 4.0 mm. Each size class (Table 1) included in the least-squares fitting algorithm had at least 10 particles. Substituting (3), (7), (8) and (9) into (6) and integrating gives the deposition depletion rate from precipitation ice.

$$\frac{dM_p}{dt} = C_2 N_p(0)\Gamma(0.65)\lambda_p^{-2} + 0.37(a\rho/\mu)^{0.5}(p_0/p)^{0.2}\Gamma(5/2 + b/2)\lambda_p^{-(5/2+b/2)} \tag{10}$$

where $\Gamma$ is the gamma function.

The accretional depletion rate of cloud water by precipitation ice is

$$\frac{dA_p}{dt} = \int_0^\infty \pi\rho \frac{L^2}{4} V q_c E_{pc} N_p(L) dL \tag{11}$$

where $q_c$ is the cloud water content and $E_{pc}$ is the collection efficiency of cloud water by precipitation ice. In the calculations below we will assume that $q_c$ is 0.1 g m$^{-3}$ based on the integrated cloud water content from the FSSP probe data (Figs. 1b and 3b).

Substituting (8) and (9) into (11) and integrating gives the accretional depletion rate

$$\frac{dA_p}{dt} = \rho\pi a q_c E_{pc} N_p(0)/4(p_0/p)^{0.4}\Gamma(b+3)\lambda_p^{-(b+3)}. \tag{12}$$

Here $E_{pc}$ is a power law function for cloud droplet diameters $< 30$ $\mu$m and is also strongly dependent on precipitation ice size and habit (Pruppacher and Klett, 1980, p. 498). Since the observed cloud droplets had mean droplet diameters of 20 to 25 $\mu$m, we will assume $E_{pc}$ is 0.5 but must recognize that $E_{pc}$ changes rapidly as conditions change. Since the cloud droplet concentration and cloud water content are typically small above the 0°C level, a small ascent of an air parcel will dramatically increase the accretion depletion rate. The increase occurs because both $q_c$ and $E_{pc}$ increase rather rapidly. Clearly, as the amount of rime increases on an ice crystal, the increased fallspeed also increases the collection efficiency.

## 4. Calculations of the precipitation process

### *a. 25 February 1983 case study*

The condensation supply rate as a function of temperature and vertical velocity ($W$) were calculated for the takeoff sounding (Part I, Fig. 2) and are presented in Fig. 5. The curves for $W$ = 20 and 40 cm s$^{-1}$ are plotted as a function of temperature. The condensation supply rates for 40 cm s$^{-1}$ are 0.6 g m$^{-3}$/1000 s at 0°C and 0.2 g m$^{-3}$/1000 s at −20°C.[2]

The $\theta_e$ = 308 and 306 K isopleths (Fig. 3, Part I) were assumed to represent streamlines of air parcels above the melting layer. Since the airflow was steady state, we can also view these streamlines as air parcel trajectories. The aircraft data at various intercept times of the streamlines are summarized in Table 3. The seg-

[2] These odd units were chosen so that the reader might have a "physical feel" for the numbers. The conventional unit for liquid water content is gm$^{-3}$ and 1000 s is ~18 min.

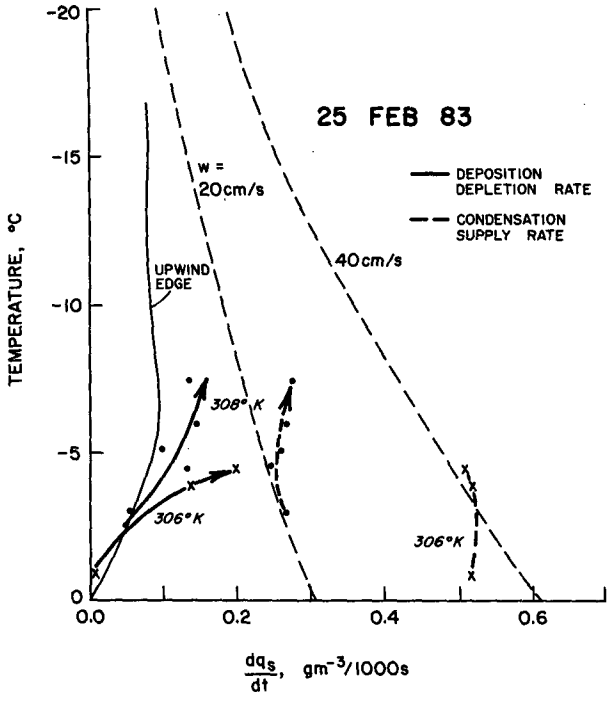


FIG. 5. Profiles of condensation supply rates and deposition depletion rates for 25 February 1983. See text for details.

ment of aircraft time was selected to be two to five minutes in length in order to obtain a statistically representative number of hydrometeors. The temperature variation for an interception of the streamline was $\leq 3$°C. The mean temperature, ($\bar{T}$), height ($\bar{H}$), pressure ($\bar{p}$) and vertical velocity ($W$) for each intercept are listed. The air parcel travel time from first intercept ($\Delta t$) are also listed. The vertical velocities were inferred by multiplying the slope of the $\theta_e$ isopleths by the component of the winds normal to the barrier ($U$) (Fig. 3d, Part I).

The condensation supply rates at each intercept time were calculated using the data in Table 3 and the values are plotted for each $\theta_e$ in Fig. 5. The condensation supply rate along $\theta_e = 308$ K was $\sim 0.3$ g m$^{-3}$/1000 s while the condensation supply rate[2] for $\theta_e = 306$ K was $\sim 0.5$ g m$^{-3}$/1000 s.

The total concentration, $N_T$, for an exponential distribution is $N(0)/\lambda$. The values of $N_T$ are listed for each spectrum in Table 3. The total concentration of cloud ice exceeds the total concentration of precipitation ice by 2 or 3 orders of magnitude. The 2D-C and 2D-P data for the number 3 intercept (Table 3) of $\theta_e = 306$ K (1956:40 to 1958:20) are presented in Fig. 6. The exponential fitted curves to the 1D-C and 2D-P data are plotted. The two spectra approximate the super-exponential distribution which was present and are clearly two separate populations of ice particles. This result justifies partitioning the ice spectra into cloud ice and precipitation ice.

From the takeoff sounding (1850 to 1905 UTC) the cloud and precipitation ice spectra were determined at a variety of temperature levels. The deposition depletion rates by cloud and precipitation ice were calculated using Eqs. (5) and (10), respectively, and the profile over the upwind edge of the barrier is presented in Fig. 5. The maximum saturation vapor pressure differential between ice and water occurs near $-15$°C. The concentrations of cloud and precipitation ice near the $-5$°C level exceed those near the $-15$°C level enough to offset the vapor pressure differential effect. The peak deposition depletion rate along the upwind edge of the barrier is $\sim 0.1$ g m$^{-3}$/1000 s near the $-5$°C level and decreases to $<0.08$ g m$^{-3}$/1000 s above the $-15$°C level.

The deposition depletion rates along the $\theta_e$ isopleths were also calculated for each cloud and precipitation ice spectrum presented in Table 3. The combined deposition depletion rates along the $\theta_e = 306$ and 308 K streamlines are plotted in Fig. 5. The deposition depletion rates from the ice particles along the upwind edge and along the streamlines are less than half the condensation supply rates. The amount of supercooled cloud water will increase or the ice crystals will multiply some more and thereby increase the deposition depletion rates or the precipitation ice will become moderately-to-heavily rimed. The data indicate that all three processes occurred. The accretional depletion rate of cloud water by precipitation ice (12) was calculated for each streamline intercept point. The values are listed in Table 3. In general, the values appear reasonable and sufficient to explain the depletion of the excess condensate by accretional growth. The calculated values were not plotted on Fig. 5 because they were highly variable. As discussed earlier, the feedback processes for accretional growth rates in these clouds are such that $q_c$ and $E_{pc}$ will likely increase enough to deplete the excess condensate and hence keep $q_c$ low. The observed cloud water content initially increased near the upwind regions of increased condensation rates. Most of the cloud water appeared to have been depleted below 0.1 g m$^{-3}$ before reaching the crest. This would indicate that the clouds responded to the increase in liquid water by developing increased depletion rates.

Examining the deposition depletion rates along the $\theta_e = 308$ and 306 K streamlines, it appears that the rates increased significantly as the streamlines ascended to the $-5$°C level. Part of this increase in deposition depletion rate was a result of increases in hydrometeor size and part was a result of increase in ice crystal concentration through ice multiplication.

### *b. 30 March 1982 case study*

The condensation supply rates (1) as a function of temperature and vertical velocity ($W$) were calculated for the takeoff sounding (Part I, Fig. 4a) and are presented in Fig. 7. The curves for $W = 20$ and 40 cm s$^{-1}$ are plotted as a function of temperature. The conden-

TABLE 3. Streamline intercept data for 25 February 1983 case study.

| Intercept | Time (UTC) | $\bar{T}$ (0°C) | $\bar{H}$ (km) | $\bar{p}$ (mb) | $W$ (m s$^{-1}$) | $\lambda_c$ (cm$^{-1}$) | 1D-C $N_c(0)$ (cm$^{-4}$) | 1D-C $N_T$ (L$^{-1}$) | 2D-P $\lambda p$ (cm$^{-1}$) | 2D-P $N_p(0)$ (cm$^{-4}$) | 2D-P $N_T$ (L$^{-1}$) | $\Delta t$ (min) | $dA_p/dT$ (g m$^{-3}$/1000 s) |
|---|---|---|---|---|---|---|---|---|---|---|---|---|---|
| | | | | | | $\theta_e$ = 308 K | | | | | | | |
| 1 | 1922:30–1925:50 | −3.1 | 2.8 | 721 | 0.22 | 296 | 70.4 | 238 | 16.6 | 0.129 | 7.8 | 0 | 0.13 |
| 2 | 1858:00–1859:40 | −5.2 | 3.1 | 690 | 0.22 | 263 | 84.1 | 320 | 12.2 | 0.039 | 3.2 | 10 | 0.10 |
| 3 | 1909:50–1911:40 | −4.5 | 3.0 | 693 | 0.23 | 319 | 164.7 | 516 | 13.4 | 0.102 | 7.6 | 21 | 0.20 |
| 4 | 1942:00–1944:30 | −6.1 | 3.3 | 695 | 0.26 | 319 | 187.2 | 587 | 25.6 | 0.083 | 3.2 | 38 | 0.02 |
| 5 | 1954:00–1956:00 | −7.5 | 3.5 | 659 | 0.27 | 340 | 165.9 | 488 | 11.4 | 0.051 | 4.5 | 50 | 0.16 |
| | | | | | | $\theta_e$ = 306 K | | | | | | | |
| 1 | 1912:00–1913:30 | −0.7 | 2.1 | 785 | 0.36 | 423 | 55.8 | 132 | 6.4 | 0.005 | 0.8 | 0 | 0.16 |
| 2 | 1945:00–1948:00 | −4.0 | 2.9 | 713 | 0.42 | 230 | 103.1 | 448 | 17.7 | 0.059 | 3.3 | 24 | 0.05 |
| 3 | 1956:40–1958:20 | −4.6 | 2.9 | 711 | 0.42 | 372 | 382.0 | 1027 | 9.5 | 0.023 | 2.4 | 27 | 0.13 |

sation supply rate for 40 cm s$^{-1}$ is 0.55 g m$^{-3}$/1000 s at 0°C and decreases to 0.30 g m$^{-3}$/1000 s at −20°C.

The $\theta_e$ = 300, 298 and 296 K isopleths (Fig. 5c, Part I) were assumed to represent streamlines of air parcels above the melting layer. The aircraft data utilized to represent the characteristics of the air parcels at various intercept times are summarized in Table 4. The vertical velocities were inferred by multiplying the slope of the $\theta_e$ isopleths by the component of the winds normal to the barrier ($U$) (Fig. 5d, Part I).

The condensation supply rates (1) at each intercept time were calculated using the data in Table 4, and the values are plotted in Fig. 7. The condensation supply rates along $\theta_e$ = 300 K decreased from 0.22 g m$^{-3}$/1000 s at −10°C to 0.16 g m$^{-3}$/1000 s at −13°C. The decrease in condensation supply rate occurred primarily because $W$ decreased from 20 to 15 cm s$^{-1}$. The condensation supply rates along $\theta_e$ = 298 and 296 K increased from ~0.25 g m$^3$/1000 s to ~0.40 g m$^{-3}$/1000 s as the streamlines ascended from −5° to −13°C and −1.5° to −9°C, respectively.

From the descent sounding (2305 to 2320 UTC) the cloud and precipitation ice spectra over the upwind edge of the barrier were determined at a variety of temperature levels. The deposition depletion rates by cloud and precipitation ice were calculated using (5) and (10), respectively. The profile of deposition depletion rate over the upwind edge of the barrier is presented in Fig. 7. The maximum deposition depletion rate occurred near the −5°C level concomitant with the peak concentration of ice particles. The peak deposition depletion rate was ~0.1 g m$^{-3}$/1000 s and decreased to <0.01 g m$^{-3}$/1000 s above the −15°C level.

The deposition depletion rates along the $\theta_e$ isopleths were also calculated for each cloud and precipitation ice spectra presented in Table 4. The combined deposition depletion rates along the $\theta_e$ = 300, 298 and 296 K streamlines are plotted in Fig. 7.

The deposition depletion rates were less than half the condensation supply rates except for the $\theta_e$ = 300 K streamline. As the 300 K streamline approached the −12°C level, the depletion rate equalled the condensation rate. The images at this point appeared to be only lightly rimed, i.e., in agreement with these calculations.

Since the deposition depletion rates increased as the streamlines ascended through and above the −5°C level, this indicates that the concentration and mean particle sizes increased along the streamline. The increased concentration of ice particles increased the deposition depletion rate but not enough to equal the

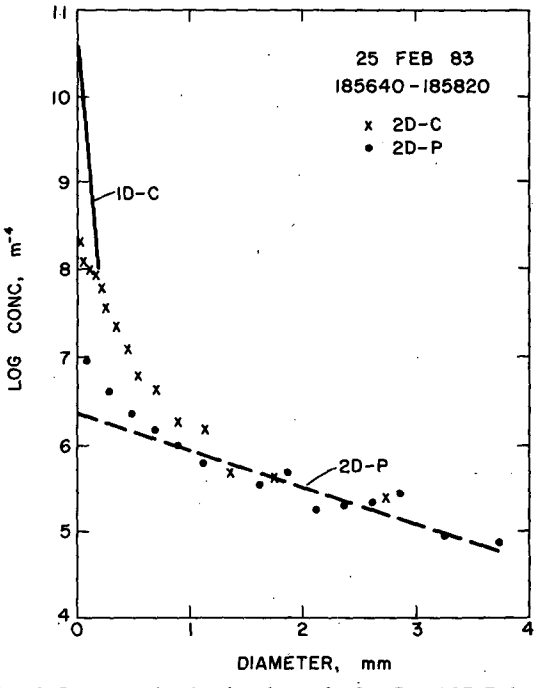


FIG. 6. Concentration by size classes for 2D-C and 2D-P data on 25 February 1983 (1856:40–1858:20). This is intercept 3 of $\theta_e$ = 306 K (see Table 3). The exponential spectra for the 1D-C and 2D-P data are drawn and labeled.

TABLE 4. Streamline intercept data for 30 March 1982 case study.

| Intercept | Time (UTC) | $\bar{T}$ (0°C) | $\bar{H}$ (km) | $\bar{p}$ (mb) | $\bar{W}$ (m s$^{-1}$) | 1D-C $\lambda_c$ (cm$^{-1}$) | 1D-C $N_{0c}$ (cm$^{-4}$) | 1D-C $N_T$ (L$^{-1}$) | 2D-P $\lambda_p$ (cm$^{-1}$) | 2D-P $N_{0p}$ (cm$^{-4}$) | 2D-P $N_T$ (L$^{-1}$) | $\Delta t$ (min) | $dA_p/dt$ (g m$^{-3}$/1000 s) |
|---|---|---|---|---|---|---|---|---|---|---|---|---|---|
| | | | | | | $\theta_e$ = 300 K | | | | | | | |
| 1 | 2311:00–2313:00 | −9.7 | 3.2 | 688 | 0.20 | 514.5 | 147.1 | 286 | 6.7 | 0.008 | 1.2 | 0 | 0.14 |
| 2 | 2244:00–2249:00 | −12.2 | 3.5 | 658 | 0.15 | 516.6 | 193.5 | 375 | 1.8 | 0.002 | 1.1 | 55 | 2.01 |
| | | | | | | $\theta_e$ = 298 K | | | | | | | |
| 1 | 2313:00–2315:00 | −5.4 | 2.4 | 757 | 0.20 | 419.8 | 189.7 | 452 | 12.8 | 0.033 | 2.6 | 0 | 0.08 |
| 2 | 2045:00–2048:00 | −9.6 | 2.7 | 725 | 0.27 | 364.8 | 144.0 | 395 | 3.0 | 0.002 | 0.7 | 52 | 0.43 |
| 3 | 2230:40–2233:30 | −13.2 | 3.5 | 658 | 0.40 | 498.6 | 387.7 | 778 | 7.0 | 0.027 | 3.9 | 100 | 0.40 |
| | | | | | | $\theta_e$ = 296 K | | | | | | | |
| 1 | 2330:00–2335:00 | −1.3 | 1.5 | 844 | 0.19 | 271.9 | 55.0 | 202 | 11.6 | 0.031 | 2.7 | 0 | 0.10 |
| 2 | 2210:00–2215:00 | −9.3 | 2.7 | 726 | 0.36 | 447.8 | 249.4 | 557 | 4.0 | 0.004 | 1.0 | 53 | 0.35 |

condensation supply rate. The images along the $\theta_e$ = 298 and 296 K streamlines appeared to be moderately-to-heavily rimed. Since the cloud water content did not increase with height, it is concluded that most of the excess condensate was depleted by the accretional growth process. The accretional depletion rates (12) were also calculated for each streamline intercept time and the values are listed in Table 4. As in the previous case they were sufficient to deplete the excess condensate.

## 5. Summary and discussion

The ice crystal characteristics in these two deep, stable orographic clouds were rather similar at corresponding temperature levels and locations with respect to the barrier. The concentration of ice particles indicated a peak of 30 to 200 L$^{-1}$ near the −5°C level as measured by the 2D-C probe. Many of the particles near the −5°C level were needles and the concentration exceeded the Fletcher (1962) curve for ice nuclei by several orders of magnitude. The peak concentration of ice crystals was lifted up and over the barrier crest as the air approached the barrier. Within the ice cloud the particles were distributed super-exponentially. This is particularly true near the −5°C level when lots of needles were present. The super-exponential distribution can conveniently and realistically be represented as two exponential distributions. The cloud ice distribution was estimated from the 1D-C probe data and the precipitation ice was estimated from the 2D-P probe data. Since the concentrations of these two exponential distributions differ by two or three orders of magnitude, they can be treated as two different populations of crystals. Descending from the −5°C level to the 0°C level, the concentration of ice particles decreases an order of magnitude by aggregation. Through the melting layer the concentration decreases another order of magnitude. This occurs because of additional aggregation but more importantly because the fallspeed increases as the low density aggregates melt and collapse into raindrops. The amount of rime on the ice crystals increases with size, temperature and proximity to the barrier.

The cloud droplet spectra were measured with a Forward Scattering Spectrometer Probe. Criteria were used to minimize artifacts from scattered ice particles. The spectra which were accepted as originating from cloud droplets were peaked and had concentrations of $\geqslant$10 cm$^{-3}$ for at least 30 s. The concentrations were greater below the 0°C level than above. Typical values

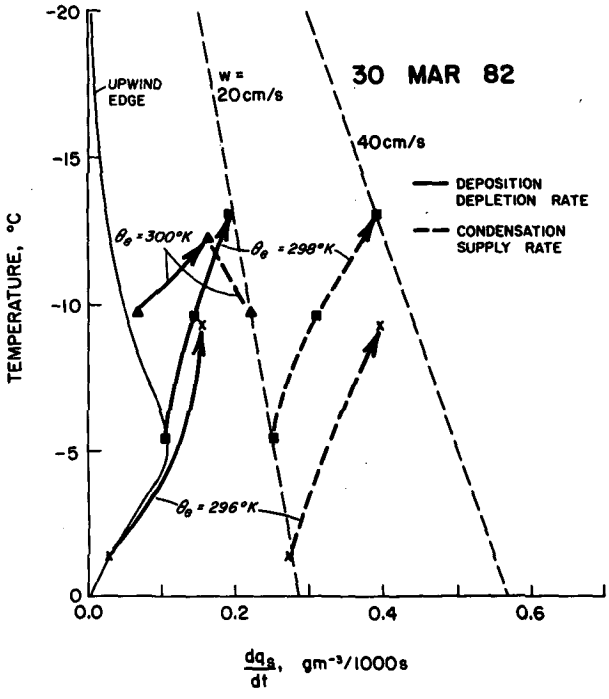


FIG. 7. Profiles of condensation supply rates and deposition depletion rates for 30 March 1982. See text for details.

below the 0°C level were 100 to 200 $cm^{-3}$. Above the 0°C level the concentrations were <100 $cm^{-3}$ and typically decreased below 10 $cm^{-3}$, especially away from the barrier. Along the barrier the concentration decreased to <10 $cm^{-3}$ near the −3°C level on 25 February 1983 and near the −13°C level on 30 March 1982. The mean diameter varied inversely with the concentration. When the concentration was >100 $cm^{-3}$, the mean diameter was <10 $\mu$m. Conversely, when the concentration was ~10 $cm^{-3}$, the mean diameter was ~25 $\mu$m. The cloud water contents in the spectra both above and below the 0°C level were ~0.1 $gm^{-3}$. This small amount of cloud water is near the minimum detectable signal for most cloud water probes.

Some possible explanations for the variations in cloud droplet spectra will next be considered. The explanations are as follows:

(i) CCN decrease with height, especially across the melting layer. Squires and Twomey (1966) and Hoppel et al. (1973) have summarized the vertical variation of CCN in continental and maritime air. In continental air the CCN decrease with altitude, while in maritime air the CCN are constant or increase with altitude, especially above the marine inversion. In continental air the surface concentration of CCN at 0.7% supersaturation is 2000 to 1500 $cm^{-3}$, while in maritime air the surface concentration is ~100 $cm^{-3}$. Above 4 km there were no systematic differences in CCN over land or ocean. Assuming the air which produced these orographic clouds had a typical maritime CCN spectra as it crossed the west coast of California, it would begin to pick up CCN from the California valley. Much of the airmass below the melting layer was in the turbulent boundary layer because of the presence of the barrier jet (Part I, Figs. 3 and 5). Above the melting layer, the airmass was stable and the turbulence level was low. Near the barrier the jet resulted in a turbulent boundary layer of ~1 km. A strong, vertical gradient in CCN might therefore be expected to develop with a strong gradient near 0°C.

(ii) The scavenging of CCN by ice is greater than scavenging by raindrops. The typical sizes for CCN are 0.1 to 1.0 $\mu$m. This size range is within the Greenfield (1957) gap in which inertial impaction and Brownian diffusion are both minimum. Within the Greenfield gap the dominant scavenging process is by phoretic forces, i.e., the thermophoretic and diffusiophoretic. They are almost always of opposite direction. For the conditions in the ice cloud (water saturation), the ice crystals are slightly warmer than the environment and hence the thermophoretic force is negative while the diffusiophoretic force is positive. Theoretical calculations indicate that raindrops in a water saturated environment (Glover et al. 1977) and ice crystals (Martin et al. 1980) in a water saturated environment both have collection efficiencies within the Greenfield gap of ~$10^{-3}$. The difference in concentration between ice crystals and raindrops suggests there should be fewer CCN in an ice cloud. Even so, it is not clear whether scavenging alone would result in fewer CCN above the 0°C level. The process is extremely complex and in need of more study.

(iii) The cloud droplets are accreted by the ice crystals. The collection efficiency of cloud droplets by ice crystals is exponentially dependent on cloud droplet size when the drop diameter is <30 $\mu$m (Pruppacher and Klett, 1980, p. 498). This fact alone does not seem able to explain the apparent distinct difference in cloud droplet concentrations across the 0°C level. Although accretion would result in a vertical gradient, it would not result in a distinct discontinuity. If the mean droplet diameter is 10 $\mu$m and cloud droplet concentration is ~10 $cm^{-3}$, then an ascent of only 100 m will result in a mean droplet diameter of ~25 $\mu$m which will be rapidly and efficiently accreted by the ice crystals.

(iv) A difference in ascent rates. The vertical velocities above the 0°C level are slightly greater than below the 0°C level. Even though the slope of the streamlines is greater below the 0°C than above, the strong vertical shear in barrier normal winds results in slightly greater ascent rates above the 0°C level than below. For most CCN spectra, the number of activated CCN is only weakly dependent on the ascent rate. Assuming the same CCN spectra above and below 0°C level a slightly greater cloud droplet concentration would result above the 0°C level than below.

Although it is not possible to explain the low concentration of cloud droplets above the 0°C level, it is clear that a maritime concentration will significantly affect the accretional depletion rate.

The relative roles of ice crystal growth by deposition and accretion will be discussed next. The ice crystal population was partitioned into cloud and precipitation ice because the concentration of cloud ice was one to two orders of magnitude greater than the precipitation ice. Exponential distributions were fitted to the cloud and precipitation ice spectra. The cloud ice was assumed to grow by only deposition because the particles were small ($L$ < 200 $\mu$m). The precipitation ice was assumed to grow by both deposition and accretion. The condensation supply rate was calculated at several points within the cloud from estimates of ascent rates (≤0.4 m $s^{-1}$). For most regions of the cloud the deposition depletion rate was less than half the condensation supply rate. Since the cloud water content was typically <0.1 g $m^{-3}$, the excess condensate was probably depleted by accretion. The accretion depletion rates were calculated. They were sufficient to deplete the excess condensate.

The last topic to be discussed is the apparent ice multiplication present in these clouds. In each storm, a layer of ice crystals with concentrations of ~100 $L^{-1}$ as observed by the 2D-C probe were measured near

the −5°C level. These concentrations are several orders of magnitude greater than the ice nuclei curve by Fletcher (1962). Many of the particles near the −5°C level were needles. There were no graupel observed but there were large ice crystals with fallspeeds of 1 to 1.5 m $s^{-1}$. The cloud droplet concentrations for diameters <13 and >24 $\mu$m were below the detectable threshold for the FSSP in the presence of such high concentrations of ice. The temperature indicates that the large ice crystal concentrations could have developed by rime-splintering. The theoretical calculations and inspection of the images suggest that riming was indeed occurring. Mossop (1985) has recently reviewed the laboratory and field evidence for the Hallett-Mossop SICP by rime splintering. Our results indicate that the Hallett-Mossop SICP occurs within the deep, stable orographic storms over the Sierra barrier. Since the layer of high ice concentrations appears to be approximately uniform along the airflow streamlines, the SICP is probably a steady, persistent process rather than occurring in a distinct region along the flow.

In summary, the most distinctive characteristic of the deep, stable orographic clouds over the Sierra barrier is the fact that the cloud droplet concentrations above the 0°C level are typically maritime. When the concentration is only 10 to 30 $cm^{-3}$ a small vertical displacement of an air parcel will result in mean droplet diameters of 20 to 30 $\mu$m. These droplet sizes are efficiently accreted by ice crystals. The accretion process not only depletes the condensate, but also results in ice multiplication when it occurs near the −5°C level. The net effect in these storms is to produce an extremely effective glaciation process in which very little supercooled water passes over the crest line. With the combination of SICP and riming, it appears unlikely for these cases that any seeding strategy could be devised which would result in a measurable increase in precipitation.

*Acknowledgments.* This research was sponsored by the Bureau of Reclamation, Department of Interior, under Contract 2-07-81-V0256. The support of Dave Reynolds, field manager, Wayne Sand and George Bershinsky, pilot-scientists, plus the other participants and colleagues in the Sierra Cooperative Pilot Project are appreciated. Glenn Gordon developed the PMS image processing programs.

## REFERENCES

Fletcher, N., 1962: *The Physics of Rain Clouds.* Oxford University Press, 386 pp.

Foote, B., and P. du Toit, 1969: Terminal velocity of raindrops aloft. *J. Atmos. Sci.*, **8,** 249–253.

Glover, S., H. Pruppacher and A. Hamielec, 1977: A numerical determination of the efficiency with which spherical aerosol particles collide with spherical water drops due to inertial impaction and phoretic and electrical forces. *J. Atmos. Sci.*, **34,** 1655–1663.

Greenfield, S., 1957: Rain scavenging of radioactive particulate matter from the atmosphere. *J. Meteor.*, **14,** 115–125.

Hallett, J., and S. Mossop, 1974: Production of secondary ice particles during the riming process. *Nature,* **249,** 26–28.

Haltiner, G., and R. W. Williams, 1980: *Numerical Prediction and Dynamic Meteorology.* Wiley and Sons, 447 pp.

Hoppel, W., J. Dinger and R. Ruskin, 1973: Vertical profiles of CCN at various geographical locations. *J. Atmos. Sci.*, **30,** 1410–1420.

Lin, Y., R. Farley and H. Orville, 1983: Bulk parameterization of the snow field in a cloud model. *J. Climate Appl. Meteor.*, **22,** 1065–1092.

Locatelli, J., and P. Hobbs, 1974: Fallspeeds and masses of solid precipitation particles. *J. Geophys. Res.*, **79,** 2185–2197.

Martin, J., P. Wang and H. Pruppacher, 1980: A theoretical determination of the efficiency with which aerosol particles are collected by simple ice crystal plates. *J. Atmos. Sci.*, **37,** 1628–1638.

Marwitz, J., 1987: Deep orographic storms over the Sierra Nevada. Part I: Thermodynamic and kinematic structure. *J. Atmos. Sci.*, **44,** 159–173.

Mossop, S., 1985: The origin and concentration of ice crystals in clouds. *Bull. Amer. Meteor. Soc.*, **66,** 264–273.

Pruppacher, H., and J. Klett, 1980: *Microphysics of Clouds and Precipitation.* Reidel, 714 pp.

Squires, P., and S. Twomey, 1966: A comparison of cloud nucleus measurements over central North America and the Caribbean Sea. *J. Atmos. Sci.*, **23,** 401–404.

Stewart, R., J. Marwitz, J. Pace and R. Carbone, 1984: Characteristics through the melting layer of stratiform clouds. *J. Atmos. Sci.*, **41,** 3227–3237.

Thorpe, A., and B. Mason, 1966: The evaporation of ice spheres and ice crystals. *Brit. J. Appl. Phys.*, **17,** 541–551.